Supporting Information

Experiments

In the majority of our experiments, all bacteria are fluorescently labeled with eGFP in order to increase the accuracy of velocity and orientation measurements. Since bacteria are closely packed, individual cell length or speed cannot be measured. We thus performed an additional series of experiments in which only 1% of cells are marked. The length of these marked cells can then be measured. Cell length distributions for different drug level are shown in Fig. S1A. The influence of the drug level appears to affect mostly the exponential tail following the small-scale dominating hump. Nevertheless, this exponential tail influences the mean cell length $L_{\rm cell}$, which is found to vary by more than a factor 2, from 6 to 14μm (inset of Fig. S1A).

In our main set of experiments (with all cells labeled), we find, at fixed drug level, a dispersion of measured velocity correlation length L_V and mean speed v of coarse grained velocity fields measured by Particle Image Velocimetry (Fig. S1B). Note that the dispersion of v values is particularly wide. Using both sets of experiments, the mean cell length $L_{\rm cell}$ and the velocity correlation length L_V are found to be almost linearly related, whereas the mean speed v is almost independent of the drug level (Fig. S1C).

These results indicate that our experiments yield quasi-independent correlation lengths and mean speeds, with only the correlation length under control of the drug level via the mean cell length $L_{\rm cell}$.

Image processing, orientation and velocity field measurements. A typical raw image (1024×1024 pixels) is shown in Fig. S2A. We first sharpen these raw images by a high-pass filter and obtain new images $I(\mathbf{r},t)$ (Fig. S2B). These images are used to extract coarse-grained orientation and velocity field.

We use the structure tensor method to find, at each pixel, the direction $\hat{\mathbf{u}}$ along which the image intensity gradient is minimal. This direction is identified with the director of the nematic field. In practice, the local structure tensor at some pixel $\mathbf{r}$ and time t is defined as

$$J(\mathbf{r},t) = \begin{bmatrix} (I_x)^2 & I_x I_y \\ I_x I_y & (I_y)^2 \end{bmatrix} \qquad [1]$$

where $I_x = \partial_x I(\mathbf{r},t)$ and $I_y = \partial_y I(\mathbf{r},t)$. These gradients are calculated by simple second-order finite difference expressions. We smooth the J tensor with a spatial Gaussian filter of width 16 pixel ($4.3\mu m$). Eigenvalues and eigenvectors of the smoothed J tensor are then computed. Finally, the local cell orientation $\hat{\mathbf{u}}$ is given by the direction of the eigenvector with the smaller eigenvalue. The orientation field corresponding to the raw image of Fig. S2A is shown in Fig. S2C and Fig. 1C of the main text.

The velocity field of bacteria in the lab frame is measured by a standard particle image velocimetry (PIV) algorithm with an interrogation window of $4.3\mu m$ (16pixel). The velocity field corresponding to the raw image of Fig. S2A is shown in Fig. S2C and Fig. 1D of the main text.

In order to perform further comparisons with model simulations, these velocity and orientation fields are interpolated on the same 78×78 grid with a spatial resolution $3.5\mu m$.

Defect detection, defect orientation and velocity. To locate defects with high accuracy, we first interpolate the measured orientation field on a fine grid (256×256) with a spatial resolution $1.08\mu m$. Around each grid point, we then measure the net change of director angle along a counterclockwise loop. Grid points with $\sim \pi$ ($\sim -\pi$) changes are identified as the cores of $+\frac{1}{2}$ ($-\frac{1}{2}$) defects.

The velocities $\mathbf{v}^+$ and $\mathbf{v}^-$ of $+\frac{1}{2}$ and $-\frac{1}{2}$ defects in the lab frame are given by the displacements of the defect cores. We also measure the "backflow" velocities $\mathbf{v}^{\pm}_{\rm back}$ at each defect core by local averaging of the velocity field $\mathbf{v}(\mathrm{r},t)$ over a disk of radius equal to $\frac{1}{3}$ of the defect core size $R^{\pm}$ around the defect core. This allows to estimate the "intrinsic" velocity of defects, i.e. their velocity in the (local) fluid frame, given by the relative velocity $\Delta\mathbf{v}^{\pm} = \mathbf{v}^{\pm} - \mathbf{v}^{\pm}_{\rm back}$. We also estimate $\hat{\mathbf{u}}^{\pm}$ the *polar* orientations of defects. For the comet-shape $+\frac{1}{2}$ defect, $\hat{\mathbf{u}}^+$ is simply given by the opposite direction of the comet tail. For the tri-axial $-\frac{1}{2}$ defect, we define $\hat{\mathbf{u}}^-$ as the axis closest to the direction of $\mathbf{v}^-$. Figures S2C,D illustrate how all these quantities are defined.

Simulations details

In our model, the continuous fluid flow and the discrete dipole dynamics are described by Eqs. (1,2) and (3,4), respectively. We simulate the dynamics of 98304 dipoles, corresponding to the global density $\rho_0 = 1.5$ chosen as explained in the main text. We use a square domain with periodic boundary conditions. We use a coarse-graining procedure to connect these two groups of equations, as illustrated by Fig. S3. We divide the computational domain into 256×256 square boxes of size Δ, equivalent to 3.5μm. The active stress $\sigma(\mathbf{r})$ exerted by dipoles in the box centered on $\mathbf{r}$ is approximated by:

$$\boldsymbol{\sigma} = f_0 \langle \hat{\mathbf{u}}_\mathbf{i} \hat{\mathbf{u}}_\mathbf{i} \rangle_\mathbf{r}.$$

where the average is taken over all dipoles i (with orientation $\hat{\mathbf{u}}_i$) located in the box. These dipoles apply a total force on the fluid at $\mathbf{r}$:

$$\mathbf{F}(\mathbf{r}) = f_0 \nabla \cdot \langle \hat{\mathbf{u}}_\mathbf{i} \hat{\mathbf{u}}_\mathbf{i} \rangle_r + \frac{1}{\Delta^2} \sum_{k \in \mathbf{r}} \sum_{l \in R_k} \mathbf{R}_{kl} \, . \qquad [2]$$

where the second term, usually negligible, arises from the short-range repulsion between dipoles, and sums through all dipoles (indexed by$k$) in the box (centered on $\mathbf{r}$) and the l dipoles are within interaction range of the kth dipole. The precise shape of the repulsive potential used has very little influence on our results. Throughout this work, we report results obtained using a simple harmonic potential: $\mathbf{R}_{ij} = C_r(\Delta - r_{ij})\hat{\mathbf{r}}_{ij}$ if $r_{ij} < \Delta$ ($\mathbf{R}_{ij} = 0$ otherwise), where r_{ij} is the distance between dipoles i and j, and $\hat{\mathbf{r}}_{ij}$ is the unit vector going from j to i.

The force field $\mathbf{F}(\mathbf{r})$ is then fed into Eqs. (1,2) in order to compute the fluid flow $\mathbf{v}$ via a spectral method. Dipole positions and orientations are then updated following Eqs. (3,4).

(To reduce the computational load, we assume that all dipoles in a box are affected by the same flow velocity $\mathbf{v}$, computed at the box center $\mathbf{r}$.)

Finally, in simulations, we fix the substrate friction coefficient α and Δ (the coarse-graining and repulsion range) to unity, which sets the simulation length and time units.

Numerical results need to be converted from simulation units to physical units before they can be compared with experimental data. To do that, we set the length unit in experiments to be the same as the measurement resolution in experiments: $\Delta = 3.5\mu m$, because coarse-graining in simulations and experiments should be performed at the same length. Simulation time unit is set to be 5.5 sec.

Description of movies

Movie S1: Velocity and orientation fields measured in experiments with (30 $\mu g/mL$ 1st column in Table S1), 45 $\mu g/mL$ (6th column in Table S1), 60 $\mu g/mL$ (12th column in Table S1) drug concentrations. See Fig. 1 for information of colormap and spatial scale. The movie is played at 30% of the recording speed.

Movie S2: We mark 10% of cells with eGFP and visualize single bacterial motion in such a system. Only a small amount of short cells (red trajectories) can go against surrounding flow (blue arrows).

Movie S3: Left panel: Experimentally measured velocity fields. Right panel: Instantaneous velocity fields reconstructed from experimental orientation fields using Eqs. 1-2 at optimal parameters.

Movie S4: Simulations of our microscopic model at the optimal parameters corresponding to the 3 experiments shown in Movie S1. The particles are dressed by a small segment oriented and colored according to their nematic axis (colormap as in Fig. 1E top).

1. Zhang R, Kumar N, Ross JL, Gardel ML, de Pablo JJ (2017) Interplay of structure, elasticity, and dynamics in actin-based nematic materials. *Proc. Natl. Acad. Sci. U.S.A.* 115(2):E124–E133.
2. Kumar N, Zhang R, de Pablo JJ, Gardel ML (2018) Tunable structure and dynamics of active liquid crystals. *Science Advances* 4(10):eaat7779.

drug level($\mu g/mL$)	30	30	30	30	45	45	45	45	60	45	45	60	60
$L_{\rm n}(\mu m)$	20.9	24.4	26.7	29.6	30.9	32.5	31.8	33.7	33.0	35.4	38.3	40.8	42.0
$L_{\rm v}(\mu m)$	28.1	29.4	32.5	34.6	37.2	39.7	40.1	40.6	40.8	43.1	46.4	49.0	51.5
$v(\mu m/s)$	32.9	23.2	31.7	40.8	42.9	50.4	29.2	34.0	44.1	44.2	43.8	44.0	54.3
$f_0/\alpha(\mu m^2/s)$	2366	1694	2551	3292	4536	6174	3807	4536	5467	5560	6471	6790	10206
$\sqrt{\mu/\alpha}(\mu m)$	26	26	26	31	32	36	34	36	36	37	38	42	46
$C_{\rm a}(s^{-1})$	0.4	0.4	0.4	0.4	0.4	0.4	0.4	0.4	0.4	0.4	0.4	0.4	0.4
$R_{\rm a}(\mu m)$	11.0	10.7	12.2	12.9	13.6	13.8	12.7	12.9	13.4	14.4	14.9	15.4	15.7
$C_{\rm v}$	0.55	0.55	0.55	0.55	0.53	0.50	0.50	0.48	0.50	0.50	0.50	0.52	0.50
$C_{\rm s}$	0.70	0.70	0.60	0.60	0.60	0.50	0.50	0.60	0.50	0.50	0.55	0.45	0.40

Table S1. Extracted model parameters from twelve experimental datasets collected at three different drug concentrations.

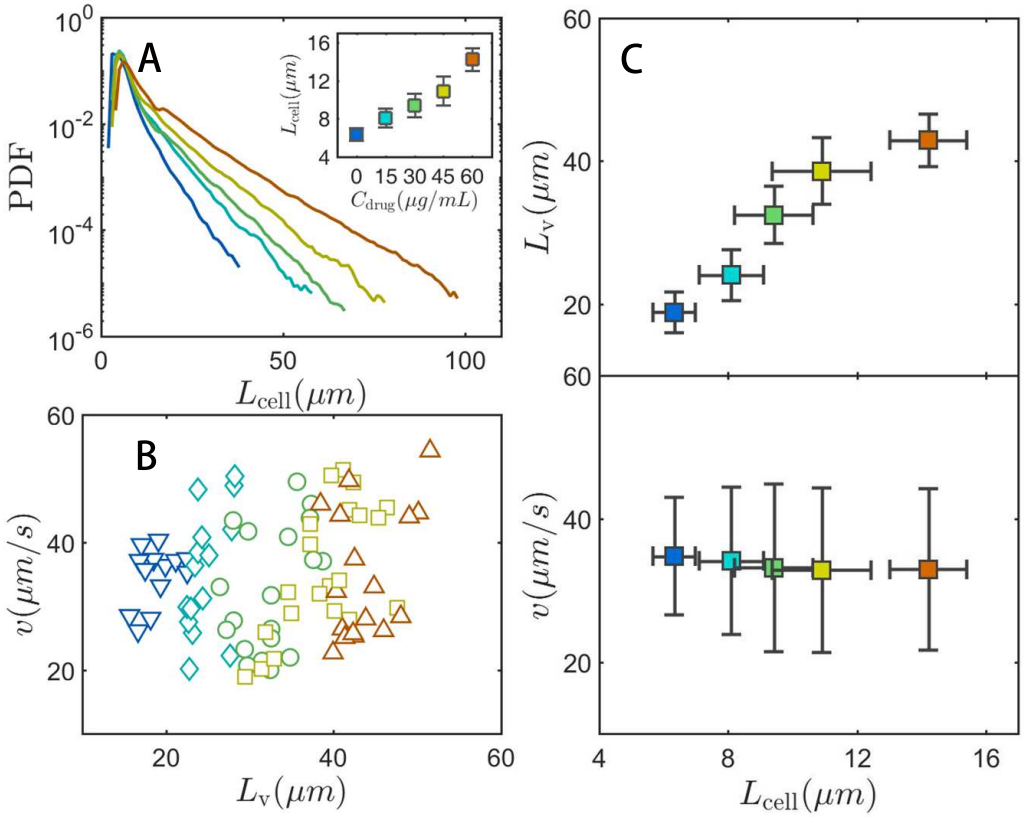

Fig. S1. (A) Cell length distribution mesured in experiments performed at various drug concentrations $C_{\rm drug}$ where only a fraction of cells is marked fluorescently. Inset: increase of average cell length with drug concentration. (B) Scatter plot of "effective control parameters": mean flow speed v versus correlation length L_V for all experiments performed with fully marked cells. (C) Variation with mean cell length of correlation length L_V and mean flow speed v, averaged over experiments performed at the same drug level. In all panels, color coding represents the drug level used.

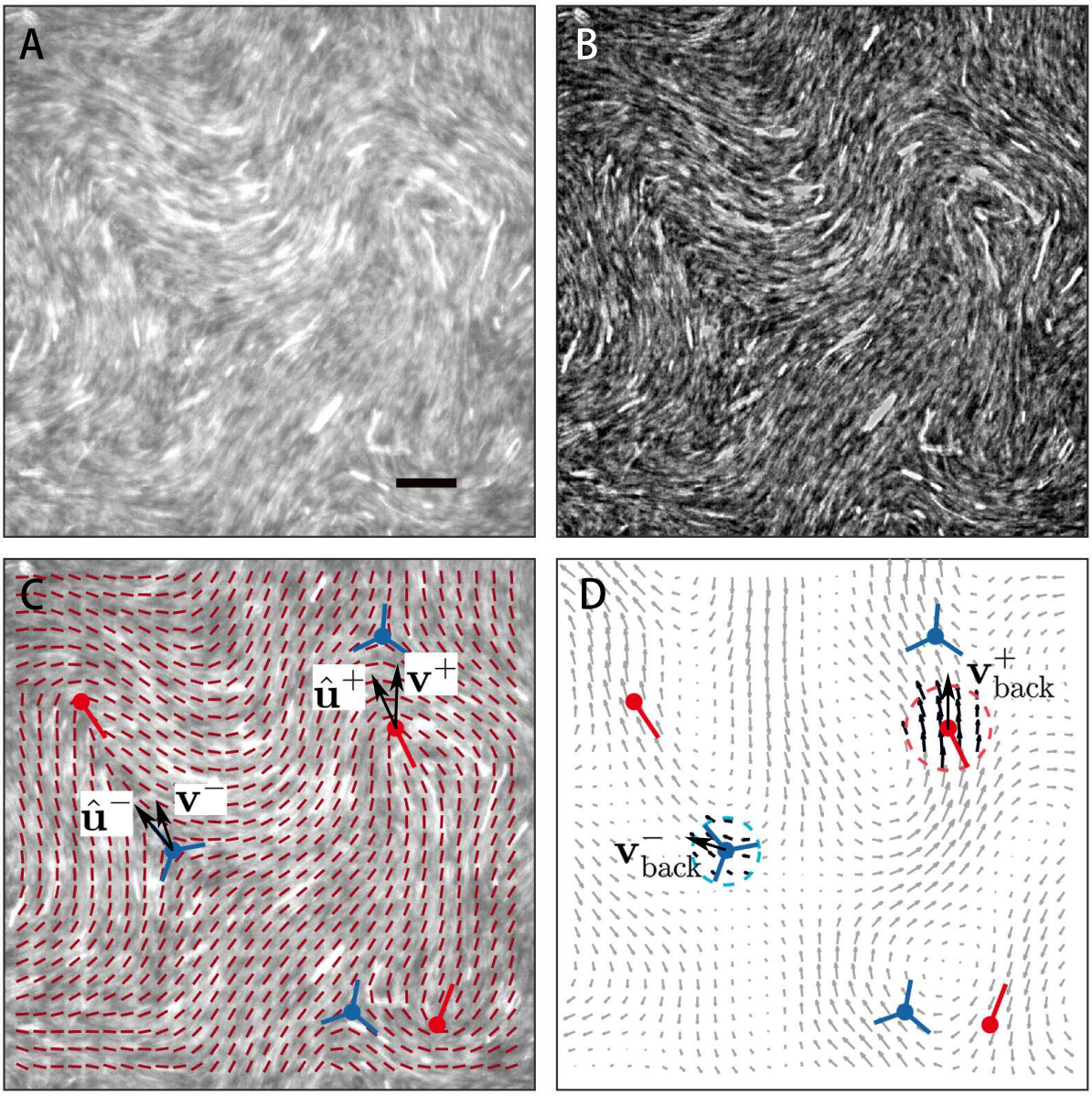

Fig. S2. (A) Raw image of fluorescently labeled cells, Scale bar is 30 μm. (B) Same image as (A), with contrast enhanced by a high-pass filter. (C) Same image as in (A), with superimposed nematic orientation field extracted from (B). Detected topological defects are indicated by red and blue symbols ($+\frac{1}{2}$ and $-\frac{1}{2}$ defects, respectively). Defect orientations $\hat{\mathbf{u}}^{\pm}$ and velocities $\mathbf{v}^{\pm}$ are also represented. (D) velocity field extracted from movie (frame corresponding to image (A)). Topological defects have been superimposed, and the flow velocity in their core region (dashed circles), $\mathbf{v}^{\pm}_{\mathrm{back}}$, is also indicated.

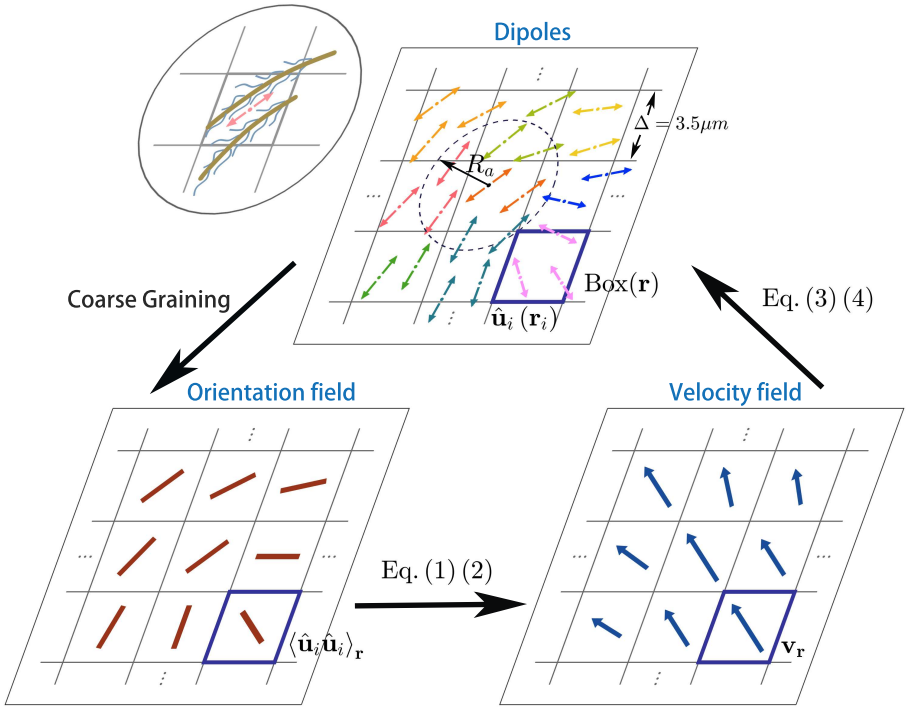

Fig. S3. Schematic diagram for the structure of the model. Averaging dipole orientations in boxes generates an orientation field on a regular grid. Eqs. (1,2) then allow to calculate the fluid flow from this orientation field. The individual dipoles positions and orientations are then updated following Eqs. (3,4). The top left inset shows that dipoles in simulation do not represent individual bacteria, but an average of cell body orientation and active forcing over a coarse-graining box.

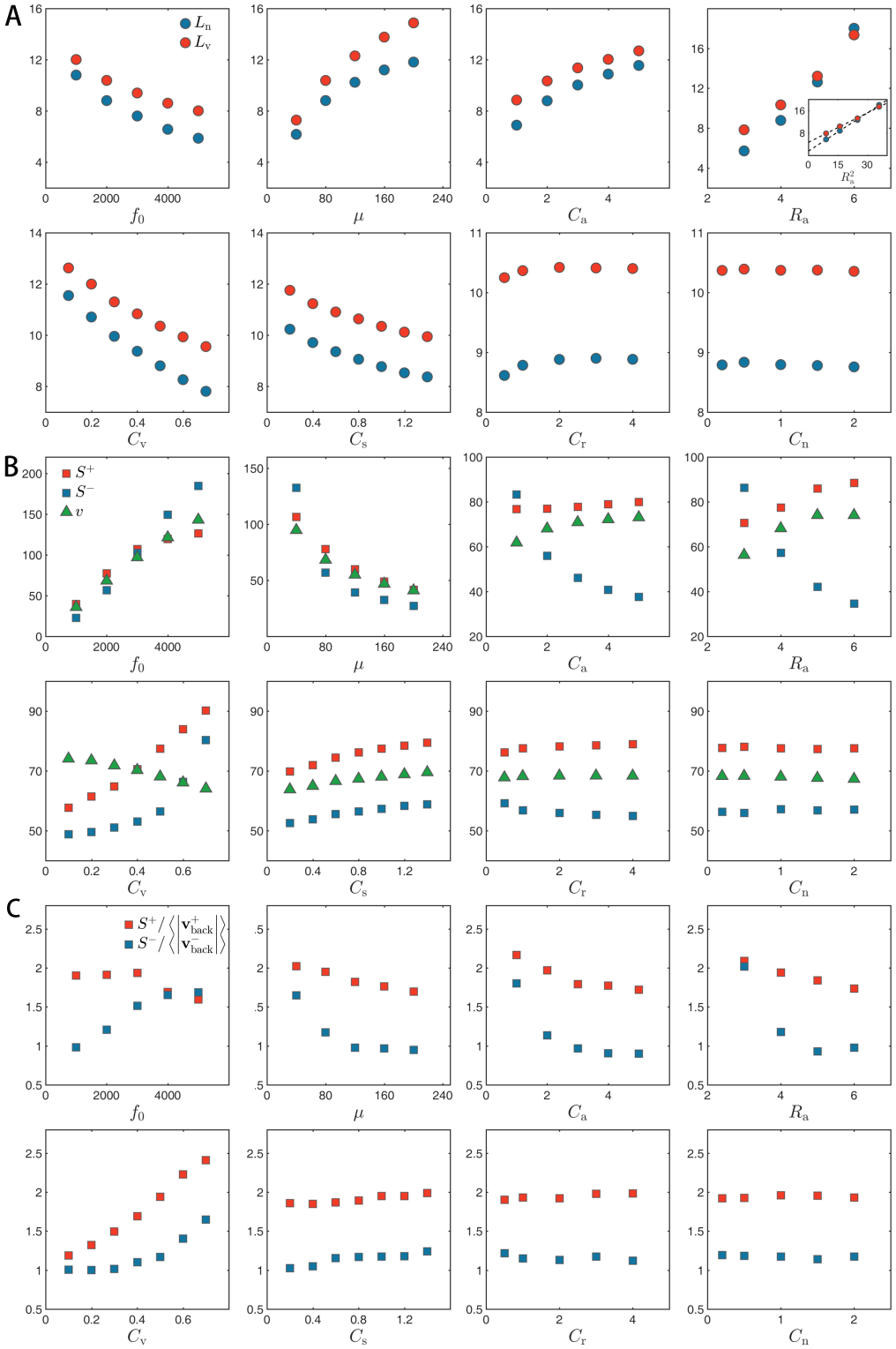

Fig. S4. Influence of individual model parameters on the quantities used in our optimization process. In each simulation, only one parameter is varied and the others are set to the following default values in simulation units: $f_0 = 2000$, $\mu = 80$, $C_a = 2$, $R_a = 4$, $C_V = 0.5$, $C_S = 1$, $C_r = 1.0$ and $C_n = 0.5$. (A) Variation of velocity (red circles) and nematic (blue circles) correlation length. Correlation lengths are mainly set by the competition between hydrodynamic instability (controlled by f_0, μ) and nematic alignment (controlled by C_a and R_a). (B) Dependence of $+\frac{1}{2}$ defect speed (red squares), $-\frac{1}{2}$ defect speed (blue squares), and mean flow speed v. The $+\frac{1}{2}$ defect speed S^+ has been divided by a factor 2.5 for an easier comparison of the 3 speeds. $+\frac{1}{2}$ defects always move faster than both global flow speed and $-\frac{1}{2}$ ones, due to active stress generated by their inherently asymmetric shape (Fig. 3A). (C) Variation of $S^\pm / \left\langle \left| \mathbf{v}^\pm_{\mathbf{back}} \right| \right\rangle$, the relative speed of defects with respect to the local flow speed at their core is shown. Those ratio increase when dipoles are sensitive to flow gradient around defect (high coupling constants C_v,C_s) or nematic interaction (C_a,R_a) weakens, consistent with experiment observation(Fig. 5C,D). All quantities in simulation units.

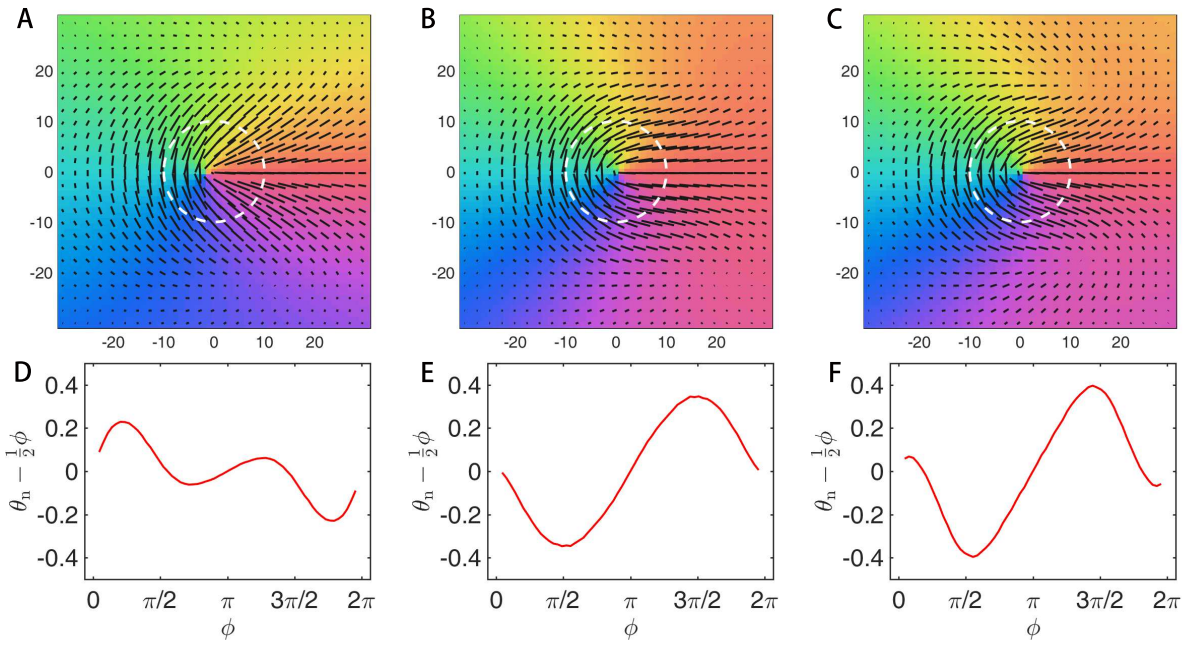

Fig. S5. Mean director field (A-C) and angular profile along a circle of radius 10 (dashed white lines) (D-F) around $+\frac{1}{2}$ defects extracted from simulations of the model with $\{C_{\rm v} = 0.1, C_{\rm s} = 1.0\}$ (A,D), $\{C_{\rm v} = 0.5, C_{\rm s} = 0.2\}$(B,E), and $\{C_{\rm v} = 0.5, C_{\rm s} = 1.0\}$(C,F). Other parameter values as in Fig. S4. The shape of the $+\frac{1}{2}$ defect changes from arrow-like to mushroom-like when we increase $C_{\rm v}$ from 0.1 to 0.5. This can be explained by the following picture: the two vortices above and below the defect center (Fig. 4C) can generate a torque that turns dipoles towards the horizontal direction. This effect is strong enough with $C_{\rm v} = 0.5$ to change the defect shape from arrow-like to mushroom-like. Such an observation also gives us a good insight on the reason why active liquid crystals often have an effectively lower bend-to-splay ratio K_{33}/K_{11} (1, 2). The strain coupling parameter $C_{\rm s}$ has a minor impact on defect shape.

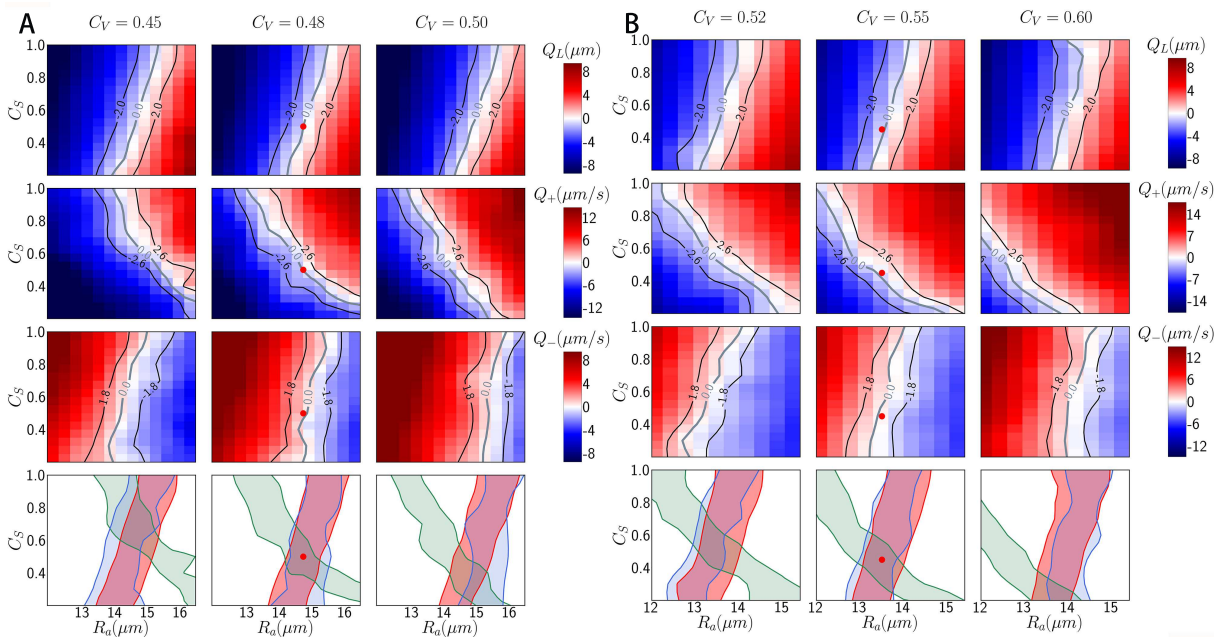

Fig. S6. Full model optimization on the same dataset as in Fig. 5, but assuming different values of the alignment strength $C_{\rm a}$. (A) $C_{\rm a} = 0.3s^{-1}$. The optimal parameter values are $\{C_{\rm v} = 0.48, C_{\rm s} = 0.5, R_{\rm a} = 14.7\mu m\}$. (B) $C_{\rm a} = 0.5s^{-1}$. The optimal parameter values are $\{C_{\rm v} = 0.55, C_{\rm s} = 0.45, R_{\rm a} = 13.4\mu m\}$. The optimal values of $C_{\rm v}$ and $C_{\rm s}$ found here are, up to our accuracy, identical to those found in the main text (Fig. 5) for $C_{\rm a} = 0.4s^{-1}$. This confirms that $C_{\rm a}$ and $R_{\rm a}$ are fully redundant.

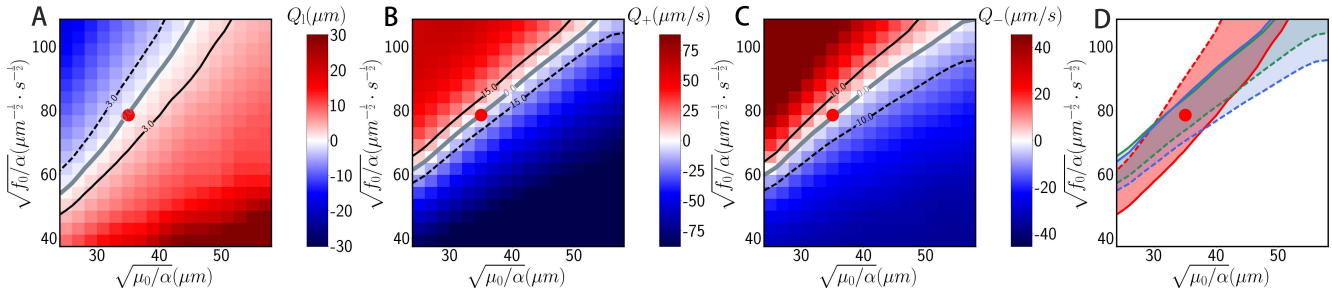

Fig. S7. "Bootstrap" check of fluid parameters f_0 and μ. After identifying all parameters in our two-step protocol, another optimization in the (f_0, μ) plane is performed, keeping all other parameters fixed at their optimal value found at the second step. (A-C): Quality functions Q_1, Q_+, and Q_- plotted in the (f_0, μ) plane. The three null lines (solid grey lines) pass by the previously determined optimal values (red dot). (D): superimposition of the regions delimited by the dashed and solid black lines in (A-C).

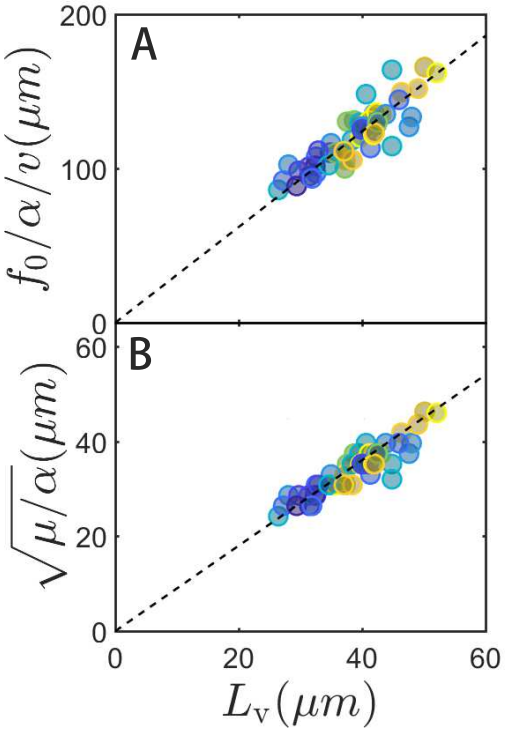

Fig. S8. Variation with correlation length of the lengthscales $f_0/(\alpha v)$ (A) and $\sqrt{\mu/\alpha}$ constructed from optimal fluid parameters for all experiment data. Symbols and colors are selected according to the mean speed v, following Fig. 2E. Optimal dipole strength f_0 still increase linearly with L_v when divided by corresponding v. This further confirms our observation in Fig. 7A and our discussion in main text.

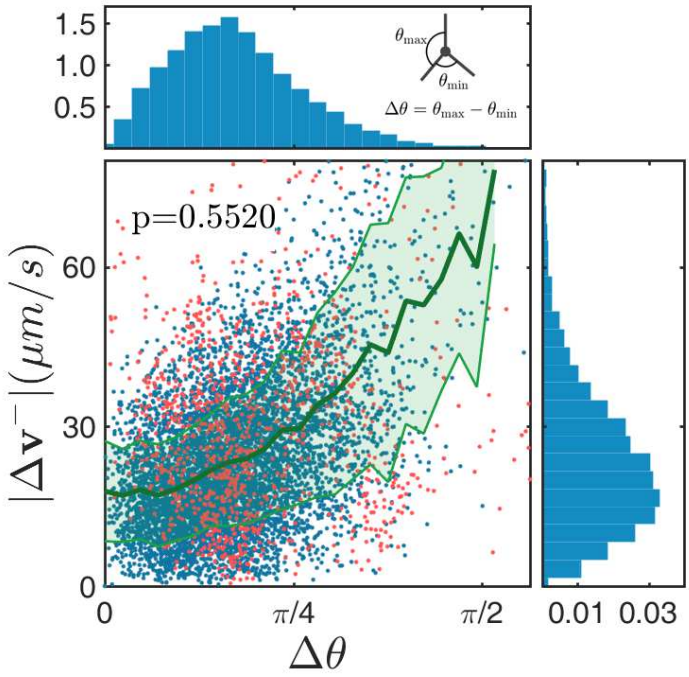

Fig. S9. Instantaneous velocity of $-\frac{1}{2}$ defects in the fluid frame is statistically correlated with how much the defect orientation fields deviate from perfect 3-fold symmetry, with a Pearson correlation coefficient $p = 0.5520$. As shown in the inset of the upper panel, we use the difference between maximum and minimum cross angles among the three branches of a $-\frac{1}{2}$ defect, $\Delta\theta$, to quantify the degree of asymmetry. Distributions of $\Delta\theta$ and $|\Delta\mathbf{v}^-|$ are plotted in upper and right boxes. Experiment and simulation data are shown by red and green dots, respectively; green lines and shadow show the mean and variation of the simulation data. Experiment and simulation data corresponding to parameters in 13th column of Table S1 are used in this figure.

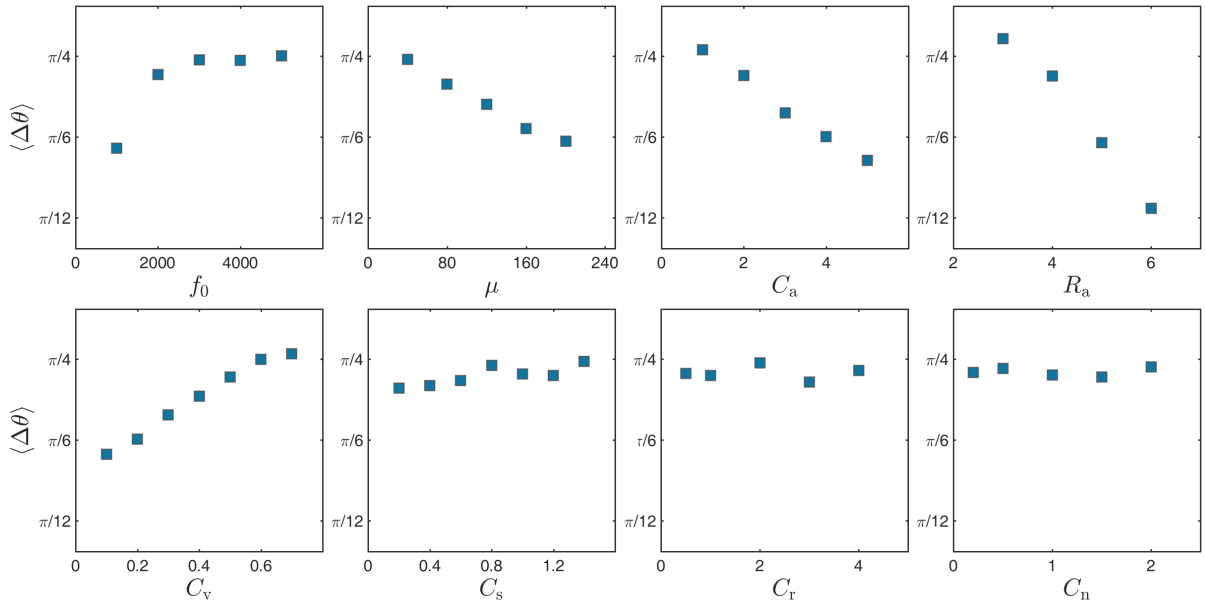

Fig. S10. Influence of model parameters on average asymmetry level of $-\frac{1}{2}$ defects $\langle\Delta\theta\rangle$. Default parameters are used: $f_0 = 2000$, $\mu = 80$, $C_a = 2$, $R_a = 4$, $C_v = 0.5$, $C_s = 1$, $C_r = 1.0$ and $C_n = 0.5$. Dependence of $\langle\Delta\theta\rangle$ on parameters is similar to that of $S^-/\left\langle\left|\mathbf{v}^-_{\text{back}}\right|\right\rangle$ shown in Fig. S4.